Stable operation of a fully energy-recovered 1-mA-class electron beam at a compact energy-recovery linac

Hiroshi Sakai,[*] Dai Arakawa, Takaaki Furuya, Kaiichi Haga, Masayuki Hagiwara,[†] Kentaro Harada, Yosuke Honda, Teruya Honma, Eiji Kako, Ryukou Kato, Yuuji Kojima,[‡] Taro Konomi,[§] Hiroshi Matsumura, Taichi Miura, Takako Miura, Shinya Nagahashi, Hirotaka Nakai, Norio Nakamura, Kota Nakanishi, Kazuyuki Nigorikawa, Takashi Nogami, Takashi Obina, Feng Qiu,[‖] Hidenori Sagehashi, Shogo Sakanaka, Miho Shimada, Mikito Tadano, Takeshi Takahashi, Ryota Takai, Olga Tanaka, Yasunori Tanimoto, Akihiro Toyoda, Takashi Uchiyama, Kensei Umemori, Masahiro Yamamoto, and Go Yoshida

High Energy Accelerator Research Organization (KEK), Tsukuba, Ibaraki, 305-0801, Japan

Nobuyuki Nishimori[†]

National Institutes for Quantum and Radiological Science and Technology (QST), Sayo-cho, Hyogo, 679-5148, Japan

Ryoichi Hajima,[¶] Ryoji Nagai,[**] and Masaru Sawamura[¶]

National Institutes for Quantum and Radiological Science and Technology (QST), Tokai, Ibaraki, 319-1195, Japan

(Received 8 September 2024; revised 3 August 2025; accepted 18 August 2025; published 26 September 2025)

A compact energy-recovery linac (cERL) has been under development at KEK to drive key accelerator technologies, demonstrate energy recovery under various conditions, and support beam applications. cERL began beam operations in 2013 to create stable, low-emittance, energy-recovered beams. The project focused on gradually increasing the current transported in a stepwise fashion while maintaining low beam losses at each step. However, the energy recovery of high-current beams is an issue that needs to be addressed. In this study, we propose a method for high-current beam tuning of approximately 1 mA under energy-recovery conditions with extremely small beam loss. We prepared a collimator and a local fast beam loss monitor to reduce the beam loss. We report successful results at approximately 1 mA, demonstrating 100.0% energy recovery with extremely small beam loss. The radiofrequency (rf) amplitude and phase varied by less than 0.02% and 0.02°, respectively. The study findings are expected to provide insights into steady beam operation for high-brightness beams and high-efficiency energy-recovery operations required for future extreme ultraviolet free-electron lasers.

DOI: 10.1103/qvpb-jsqx

[*]Contact author: hiroshi.sakai.phys@kek.jp

[†]Present address: National Institutes for Quantum Science and Technology (QST), Sendai, Miyagi, 980-8579, Japan.

[‡]Retired from High Energy Accelerator Research Organization, KEK, 1-1 Oho, Tsukuba, Ibaraki 305-0801, Japan.

[§]Present address: Michigan State University, East Lansing, Michigan 48824, USA.

[‖]Present address: Institute of Modern Physics (IMP), Chinese Academy of Sciences, Lan Zhou, Gan Su, 730000, China.

[¶]Present address: National Institutes for Quantum Science and Technology (QST), Kizugawa, Kyoto, 619-0215, Japan.

[**]Present address: National Institutes for Quantum Science and Technology (QST), Chiba, Chiba, 263-8555, Japan.

I. INTRODUCTION

The energy-recovery linac (ERL) can accelerate high-current beams with low emittances and short bunches. The ERL concept was proposed by Tigner [1], based on the following principles: The high-current beam generated by the high-brightness electron gun is first accelerated by the accelerating cavities and recirculated. The beam returns to the same cavities and is decelerated by the same accelerating cavities. By decelerating at the same cavities, this beam energy is stored in the same accelerating cavities and "reused" for the acceleration of the beam from the injector. This energy-recycling scheme is a key feature of the ERL. In particular, using a superconducting cavity with no cavity-wall losses for accelerating cavities enables approximately 100% energy-recovery operation of high-current

continuous-wave (cw) beams. Compared with storage rings, ERLs can produce short bunches and are not limited to an equilibrium emittance governed by synchrotron radiation quantum excitation. In addition, they can support higher beam currents compared with single-pass linacs. Furthermore, the technology is sustainable and can significantly reduce the operating power by reusing the beam power in superconducting cavities.

ERL applications vary widely [2]. For example, using ERL for collider accelerators in high-energy [3] and nuclear particle experiments [4,5] has been proposed. Furthermore, extremely high-intensity free-electron laser (FEL) light sources, which are not possible with existing light sources, have been proposed [6,7]. In addition, ERL-based compact x-ray sources using laser Compton scattering [8] and THz light source applications have been proposed [9]. The key technologies for these applications mentioned above include a high-brightness electron gun with low emittance and high current, a superconducting accelerating cavity for energy recovery, and a beam-handling technology for energy recovery with extremely small beam loss.

Various test facilities have been constructed worldwide to improve energy-recovery technologies for high-brightness, high-current beams. In the 2000s, the Japan Atomic Energy Agency [10] in Japan and the Jefferson Laboratory (JLab) [11] in the United States conducted energy recovery using superconducting cavities in infrared FEL experiments as the superconducting technology matured. For example, JLab achieved a maximum energy recovery of 9 mA at 150 MeV. During its operation, the beam instability of the higher-order mode beam breakup (HOM-BBU) appeared at a few milliamperes. The effect of the beam emittance on HOM-BBU instability was observed. Although stable beam operation has been a challenge for higher-current cw beam operations with superconducting cavities, ERL operation has been successfully performed using energy recovery with normal-conducting cavities in a recuperator [12], in which a current of 30 mA was recovered. However, the wall loss of the cavity due to normal conduction was very large, and the acceleration gradient was very low. Notably, a multiturn ERL is a more cost-effective operation style owing to the reduced superconducting cavity section requirements and lower construction and operating costs. Some facilities successfully operate with a low-current beam for multiturn ERL operations [5,13]. High-brightness electron guns have been developed at CBETA, the ERL test machine at Cornell University, achieving an emittance of less than 1 mm mrad with a 390 kV dc electron gun at a high beam current of 65 mA [14]. Consequently, the energy recovery of high-current beams is an issue that needs to be addressed. In particular, the stable energy-recovery operation of a high current without beam loss, even at high gradients, in a superconducting cavity, is of utmost importance for developing ERLs worldwide. For example, radiation due to beam loss during the energy-recovery operation causes damage and/or heat load to the components of the beamline. Furthermore, uncontrolled beam loss is a significant problem in the design of radiation shields, which are used for protection during beam operations. Based on these limitations, a compact ERL (cERL) was constructed to ensure stable, high-current ERL beam operation.

In this study, we propose a method for high-current beam tuning at approximately 1 mA under energy-recovery conditions. We prepared a collimator and a local fast beam loss monitor to reduce the beam loss. The results demonstrated 100.0% energy recovery with extremely small beam loss, addressing existing gaps regarding the energy recovery of high-current beams.

The remainder of this paper is organized as follows: Sec. II provides a brief description of the cERL. The beam-tuning methods for reducing the beam loss of a cw high-current beam under energy recovery are also introduced, explaining the important components of the cERL in Sec. II. Section III presents the measurement results of the beam parameters and energy-recovery efficiency under approximately 1 mA stable beam operation. Section IV discusses the correlation between the radiation dose outside the radiation shield during energy recovery and the energy-recovery efficiency, as well as the beam parameters under energy-recovery conditions. Section V concludes the study.

II. MATERIALS AND METHODS

This section presents a brief overview of the cERL, reviewing the critical components for high-current beam operation under energy-recovery conditions. In addition, it presents a method for high-current beam tuning at approximately 1 mA under energy-recovery conditions.

A. Experimental setup of cERL

1. Overview of compact ERL

The cERL was constructed at the High Energy Accelerator Research Organization (KEK) in 2009 to study the feasibility of a future 3 GeV ERL light source [15].

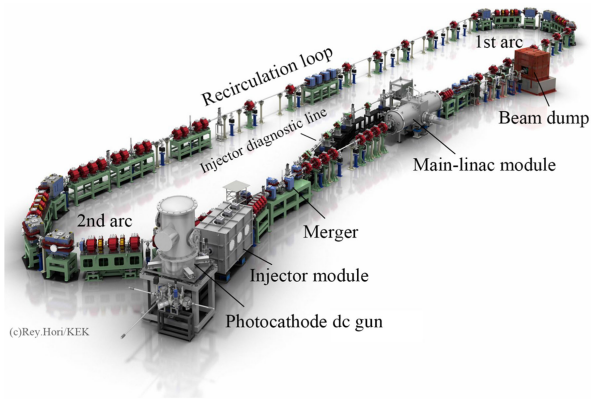

FIG. 1. Schematic view of the cERL [15].

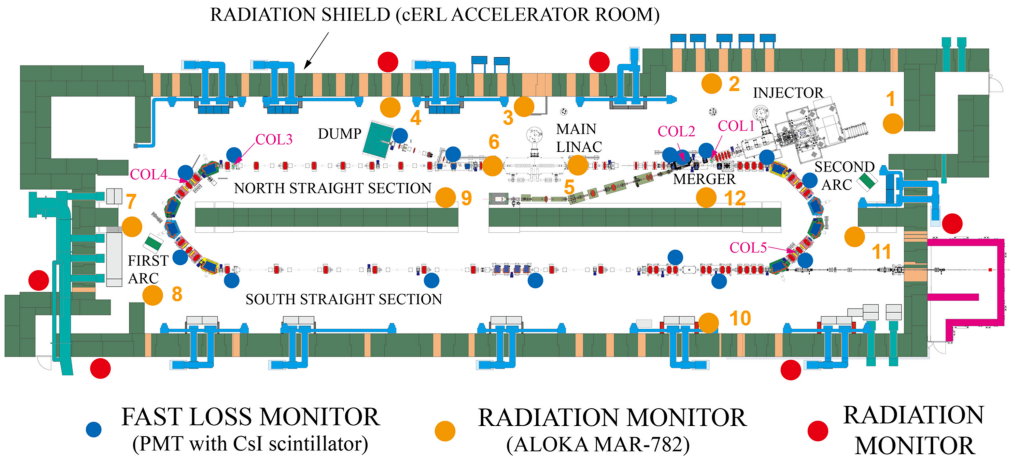

FIG. 2. Setting of local fast loss monitors (blue circles). The locations of the local collimators are expressed as COL1, 2, 3, 4, and COL5. ALOKA radiation monitors (yellow circles) are also shown with numbering [15].

Figure 1 shows a schematic of the cERL. The cERL comprises a high-brightness photocathode dc gun [16] capable of producing ultralow emittance beams at a high average current for long periods, a green 1 W power laser for irradiating the photocathode, an injector cryomodule with three two-cell 1.3 GHz superconducting cavities [17], a main-linac superconducting cavity with two nine-cell 1.3 GHz superconducting cavities, where energy recovery is performed [18], a recirculation loop for energy recovery to maintain high beam quality, and a beam dump for the decelerated beam. A main-linac superconducting cavity was designed to suppress the HOM-BBU, which made the beam unstable in the JLab-FEL for high-current beam operation [11], for a beam energy-recovery condition of more than 600 mA [19]. Further details of cERL can be found in [15], along with the description of 10-μA cw beam commissioning in 2013.

2. *Critical components for cw beam operation*

This section describes the critical components for cw beam operation at 1 mA. Figure 2 shows the radiation monitor and collimator system settings for high-power cw beam operation. For high-current cw beam operation under highly efficient energy-recovery conditions, the small beam loss along all beamlines must be minimized. We installed five beam collimators to achieve such low beam losses, as shown in Fig. 2. The detailed injector beamline with dispersion functions is shown in Fig. 3. Each collimator had four water-cooled copper rods, which were inserted in both horizontal and vertical directions, as shown in Fig. 4. The beam halo, defined as a collection of low-density particles around the core of the transverse beam distribution, and the beam tail, defined as a collection of low-density particles around the core of the longitudinal beam distribution, are primarily eliminated by two collimators, COL1 and COL2, located in the low-energy section of a 3-MeV injector beam, as shown in Fig. 3. The remaining beam halos were eliminated by three other collimators: COL3–COL5. Each collimator was locally shielded with a 20-mm-thick lead jacket and lead blocks. The tolerable amounts of beam losses were 1 and 10 μA (at 6 MeV) for the local shields at the COL1 and COL2 collimators, respectively, and 50–100 nA (at 26 MeV) at the COL3–COL5 collimators.

We prepared a local fast beam loss monitor to detect beam loss and cut the drive laser of the electron gun for safety purposes. This monitor comprises a photomultiplier tube (PMT Hamamatsu, R11558) and a CsI (pure)

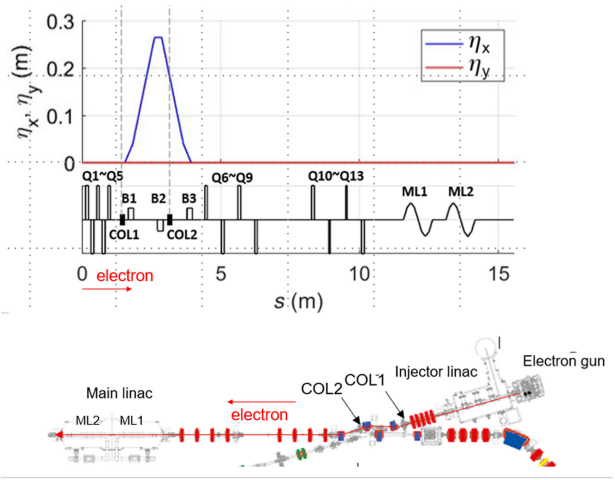

FIG. 3. Top: plot of the dispersion function along the cERL beamline from the exit of the injector cryomodule to the end of the main linac. The horizontal axis shows the distance from the exit of the injector cryomodule to the end of the main linac. The main components, including collimators (COL1 and COL2), are shown at the bottom of the top figure. The vertical axis shows the dispersion functions along the beamline shown in the bottom figure. The blue (red) line shows the horizontal (vertical) dispersion functions, respectively. Bottom: expanded view of the injector part from the electron gun to the main linac with the merger. The line shows the beamline from the gun to the main linac, including the components.

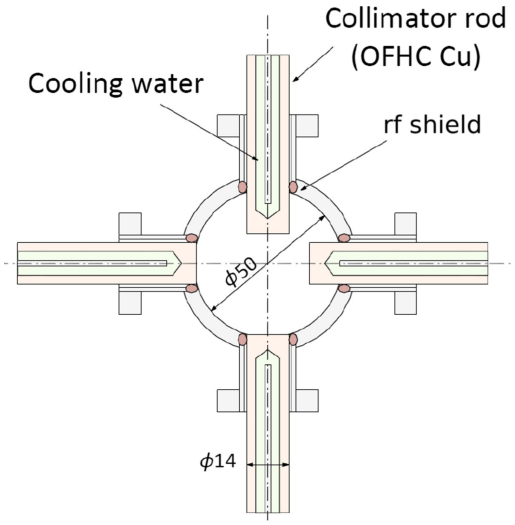

FIG. 4. Cross section of collimators (COL1 and COL2). The horizontal rods (left and right collimator rods) are set at the upstream side of the collimator, and the vertical rods (upper collimator rod and lower collimator rod) are set at the downstream side of the collimator along the beamline. The distance between the horizontal and vertical rods along the beamline is 24 mm. The outer diameter of the rod is 14 mm. The upper and lower rods and the left and right rods are set so that they do not collide with each other.

scintillator with dimensions of $25 \times 10 \times 10$ mm, designed to observe the local beam loss and interlock with the beam within 10 μs. We prepared 16 local fast beam loss monitors in the cERL, denoted by the solid blue circles in Fig. 2. These loss monitors were placed approximately 10 cm away from the cERL beamline.

cERL is shielded by a 1-m-thick concrete block roof and 1.5-m-thick concrete block walls for radiation protection purposes. The 12 radiation monitors (Hitachi Aloka Medical, MAR-782) (referred to as the "ALOKA radiation monitor" hereafter) were located in a cERL accelerator denoted by solid yellow circles, as shown in Fig. 2. Furthermore, we directly measured the radiation on the cERL roof.

The beam was rastered at high speeds by a fast-steering magnet immediately before the beam dump to prevent localized heating due to the effect of a high-current beam on the beam dump.

B. Method of beam tuning toward cw 1 mA beam under energy-recovery conditions

1. Optics and beam-tuning method

For beam tuning, we first used the burst mode before cw beam operation. In this burst mode, burst lengths of 0.1–1.2 μs and a burst repetition rate of 5 Hz were used. This short burst length enabled beam profile monitoring. The bunch charge was typically 0.7 pC at 1.3 GHz beam repetition. Beam optics matching was performed upstream

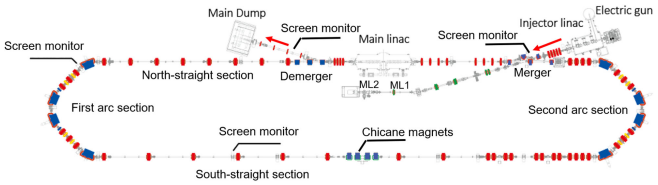

FIG. 5. The beamline configuration on the cERL.

from the electron gun [20]. The energy of the injector part was adjusted by fine-tuning the amplitude and phase of the injector cavity; it was determined by the bending magnet of the merger to the circumference section, as shown in Fig. 5. The energy of recirculation was obtained as follows: First, the beam energy was optimized to set the design voltage of ML1, as shown in Fig. 5, by scanning the phase to the on-crest condition. Second, we set the design voltage of ML2, as shown in Fig. 5, using the same method as that for ML1. For ML1 and ML2 adjustments, the beam energy was measured using the position of the screen monitor immediately after the bending magnet at the entrance of the first arc section to set the on-crest condition. After tuning the beam optics in the recirculation loop without bunch compression in the arc section, the beam was decelerated using ML1 and ML2 to achieve energy recovery. After passing through ML1 and ML2, the beam energy was minimized by changing the path length of the circumference of the cERL. The path length was altered primarily by changing the beam optics in the second arc section and the chicane magnets, as shown in Fig. 5. The beam energy after deceleration was measured using a screen monitor immediately after bending the demerger section. The bending angle of the bending magnets in the demerger was set to match the energy of the injected beam. The main-linac cavities, ML1 and ML2, were detuned, and the injected beam was directly threaded to the dump, allowing the demerger dipoles to be set.

2. Reduction of unexpected beam halo in a 1 mA cw beam operation using collimators

A beam produced from a dc gun is accelerated once around the recirculation loop. Unwanted tails or halos in the beam are also transported, resulting in beam loss. In particular, owing to the time response of the cathode material, the beam tail is produced after a short laser pulse and forms a beam halo in the transverse direction because the tail experiences different accelerating voltages compared with the core of the beam [21].

The beam halo and tail were cut by the collimator before the main-linac acceleration to reduce radiation loss. Therefore, we used COL1 and COL2 to cut the beam halo and tail. The tail of COL2 can be cut off owing to the finite dispersion function at the COL2 position. However, to cut the tail more efficiently at the COL1 positions, which have no dispersion function, the orbit of the injector cavity was

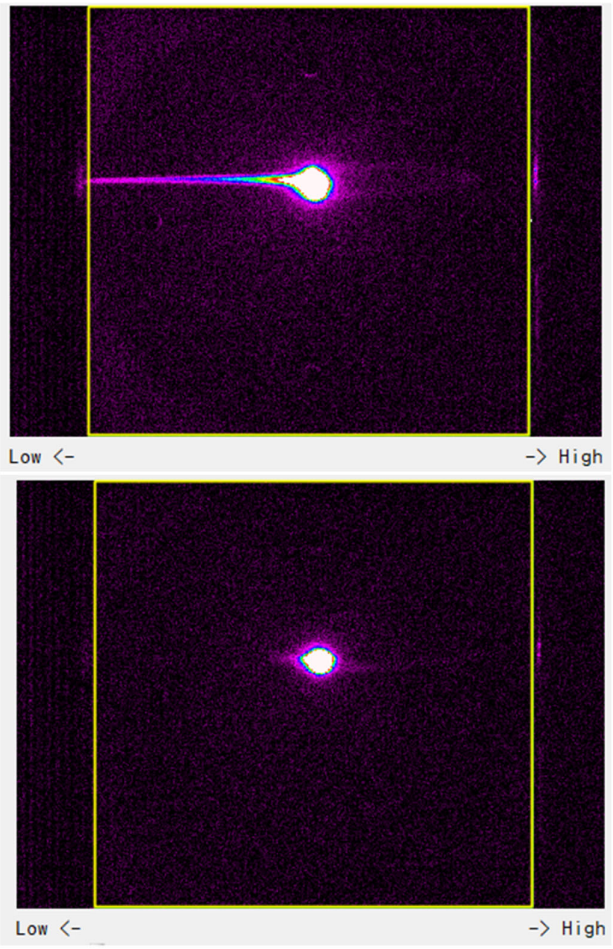

FIG. 6. Top: beam profile on a screen monitor, where the dispersion is approximately 0.23 m after the COL1 position just before entering the merger section and before inserting the collimator (COL1). Bottom: beam profile on the same screen monitor after inserting collimator (COL1). In both figures, the beam intensities in the core of the measured beam profile are saturated to emphasize the beam halo.

intentionally threaded at a finite angle so that the tail was kicked by the injector cavity field. Figure 6 shows an example of beam collimation. The beam profiles were measured at the position where the dispersion was approximately 0.23 m after the COL1 position. The low-energy tail part of the beam was successfully reduced using the vertical collimator COL1, as shown in Fig. 6. Notably, we successfully cut the tail at the COL2 position. However, as shown in Fig. 6, the beam tail was kicked by the injector cavity field, and the longitudinal beam profile was projected onto the larger vertical transverse beam profile such that the vertical collimator in COL1 could cut the beam tail more effectively. We also conducted detailed, precise collimator tuning using a fast-loss monitor while monitoring the beam current of the beam dump. Figure 7 shows the typical tuning of the collimator at COL2. After setting a length of a few millimeters from the beam center, the

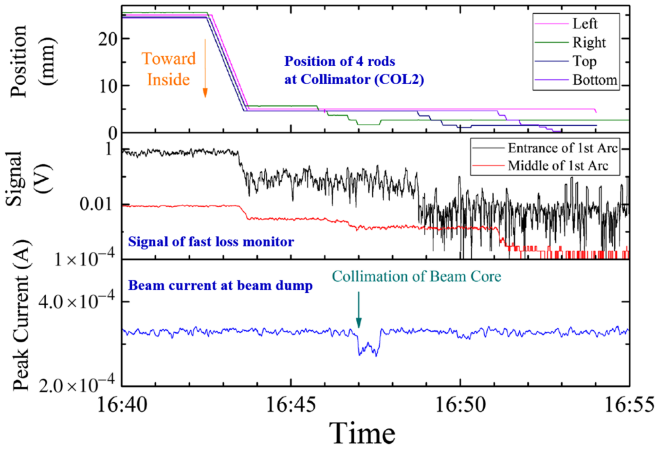

FIG. 7. Top: position of four rods at a collimator (COL2). Middle: measured signal of a fast-loss monitor under collimator tuning. Bottom: beam current at beam dump under collimator tuning. The horizontal axis shows the elapsed time.

measured signals of the fast-loss monitor reduced drastically, as shown in Fig. 6. We also monitored the beam current at the beam dump to avoid scraping the beam core during collimator tuning. COL3, COL4, and COL5 were also used to reduce beam loss, if necessary.

After sufficiently reducing the loss in burst mode, the operation was switched to cw mode. The laser intensity of the electron gun increased gradually, and the current increased while ensuring that the ALOKA radiation monitor did not exceed the threshold value. The BPM, vacuum, and power consumption of the main superconducting acceleration cavity during operation were monitored. However, the beam current wobbled slightly. The operation was conducted at approximately 0.9 mA to prevent the current from exceeding 1 mA for radiation permission purposes. This beam was operated such that it hit the entire beam dump via the fast-steering magnet immediately before the beam dump.

III. EXPERIMENTAL RESULTS

A. Parameters of the energy-recovery condition

Three experimental energy-recovery runs of a 1-mA-class beam were performed, with the parameters listed in Table I. Runs 1 and 3 are the energy-recovery operation parameters when the total energy is 20 MeV and the injector energy is 2.9 MeV. Run 1 was operated at 1.3 GHz with 0.7 pC/bunch. Meanwhile, Run 3 was operated during an x-ray generation experiment in laser Compton scattering, with a repetition rate of 162.5 MHz and a high charge of 5.5 pC/bunch. Conversely, Run 2 shows the energy-recovery operation parameters when the total energy is lowered to 17.5 MeV. For Run 2, the energy ratio in the merger section was 1:6, which is smaller than the energy ratio of 1:7 in Runs 1 and 3. Notably, sufficiently large vacuum chamber apertures were required at both the

TABLE I. Beam parameters for an approximately 1-mA cw energy-recovery operation.

Parameters	Run 1	Run 2	Run 3
Beam repetition rate (MHz)	1300	1300	162.5
Bunch charge (pC)	0.7	0.7	5.5
Gun HV (kV)	390	500	390
Injector energy (MeV)	2.9	3.0	2.9
Energy of recirculation loop (MeV)	20.0	17.6	20.0
Momentum ratio between the injector and recirculation loop	1:7	1:6	1:7

merger and demerger to allow beam transportation without beam loss at energy ratios of 1:7 and 1:6.

B. Measurement results of beam emittance and energy spread

Before the cw operation, we performed beam optics matching, as described in Sec. II B 1. The typical measurement results of the beam size after beam tuning and optics matching in Run 1 are shown in Fig. 8. The horizontal and vertical beam sizes measured at each screen monitor on the cERL beamline in Run 1 were approximately consistent with our setting optics, assuming normalized emittances of 0.3 mm mrad (for 0.7 pC).

Table II lists the results of the normalized emittance measurements for Runs 1–3. The normalized emittances were measured by scanning the quadrupole magnet in front of the monitor screen located in the south-straight section, as shown in Fig. 5. These normalized emittances were measured after optical matching, before changing the cw energy-recovery beam operation. For a low-charge beam operation of 0.7 pC/bunch in Runs 1 and 2, we achieved the lower emittance of 0.3–0.4 mm mrad. In the case of the high-charge operation of the 5.5 pC/bunch in Run 3, we successfully transported through the system without degradation of the 1–2 mm mrad produced at the gun.

In addition, we measured the energy spread using a screen monitor positioned at the entrance of the first arc section with a dispersion function of 0.49 m. The root mean square (rms) measured beam size on this screen monitor was 0.36 mm. From these measurements, we estimated a measured rms energy spread of less than 0.07% on all three runs.

TABLE II. Measured normalized emittances at the south-straight section for three runs.

Measured emittance (mm mrad)	Run 1	Run 2	Run 3
Horizontal	0.259 ± 0.005	0.406 ± 0.008	2.11 ± 0.17
Vertical	0.267 ± 0.092	0.256 ± 0.014	1.09 ± 0.05

C. Measurement results of energy-recovery efficiency

Energy recovery was conducted at the main linac to achieve a high-current beam operation of the recirculation loop. No energy was recovered at the injector section. The primary function of the ERL is to recover energy without losing beam energy in the recirculating loop. Therefore, a high energy recovery efficiency of the main linac is crucial for achieving a high-power energy recovery linac with minimal beam loss. The energy recovery efficiency of the main linac ($\varepsilon_{\mathrm{rf}}$) is given by Eq. (1) [22]

$$\varepsilon_{\mathrm{rf}} = (P_{\mathrm{rf,acc}} - P_{\mathrm{rf,load}})/P_{\mathrm{rf,acc}}. \quad (1)$$

This is defined as $P_{\mathrm{rf,acc}} = V_{\mathrm{c}} \times I$. V_{c} is the total accelerating voltage on the main linac, and I is the beam current through the main linac. $P_{\mathrm{rf,load}}$ is the remaining power that is not recovered owing to beam loading. $P_{\mathrm{rf,load}}$ is equal to $P_{\mathrm{rf,acc}}$ when the energy is not recovered. Conversely, a 100% energy recovery efficiency of the main linac is obtained when beam loading in the ERL mode vanishes completely. This implies that the rf power to the main-linac cavities should not change during energy recovery and should not depend on the beam current. If the energy recovery is not perfect, we can observe a difference in $P_{\mathrm{rf,load}}$ with and without the beam during the energy recovery operation.

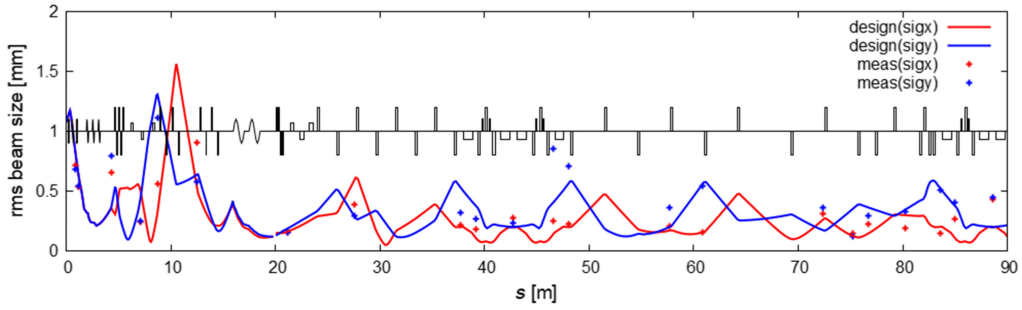

FIG. 8. The beam optics of the cERL beamline from the electron gun to the second arc section. The solid red (blue) line shows the horizontal (vertical) beam size calculated by our beam optics under conditions of 0.77 pC/bunch and 0.3 mm mrad emittances. The dotted red (blue) points show the measured horizontal (vertical) beam size at each screen monitor on Run 1.

We can measure the change in $P_{\mathrm{rf,load}}$ in each cavity with and without the beam during beam operation. $P_{\mathrm{rf,load}}$ was expressed as the change in difference $(P_{\mathrm{in,cav}} - P_{\mathrm{ref,cav}})$, where $P_{\mathrm{in,cav}}$ shows the input power to each main-linac cavity and $P_{\mathrm{ref,cav}}$ shows the reflected power from each main-linac cavity. We measured the changes of $(P_{\mathrm{in,cav}} - P_{\mathrm{ref,cav}})$ of cavities of ML1 and ML2 when the beam current (I) increased approximately 1 mA. Finally, $P_{\mathrm{rf,load}}$ through the main linac was estimated. The energy recovery efficiency ($\varepsilon_{\mathrm{rf}}$) in Eq. (1) is rewritten during the cw beam operation at the cERL as

$$\varepsilon_{\mathrm{rf}}(\%) = (1 - (P_{\mathrm{in}} - P_{\mathrm{ref}})/P_{\mathrm{rf,acc}}) \times 100\%, \qquad (2)$$

where the beam power is expressed as $P_{\mathrm{rf,acc}} = (V_{\mathrm{c1}} + V_{\mathrm{c2}}) \times I$, with the ML1 cavity voltage (V_{c1}), ML2 cavity (V_{c2}), and P_{in} (P_{ref}) expressed as the sum of the $P_{\mathrm{in,cav}}$ ($P_{\mathrm{ref,cav}}$) of the ML1 and ML2 cavities, respectively. We stably operated by monitoring the rf field using a pickup monitor with low-level radio frequency (LLRF) control. The rf amplitude and phase were stable to within 0.02% and 0.02°, respectively. Owing to this LLRF control, the beam energy in the recirculation loop of the cERL was stabilized within an rms of 0.01% [23].

Figure 9 shows the history of the beam current during the energy recovery of an approximately 1-mA cw beam in Run 2. We observed fluctuations in the measured beam current at the gun at approximately 1 mA, as shown in Fig. 9. Considering the measurement errors of both beam currents, the beam currents of the injection beam and dump section were transported with almost no loss, as shown in Fig. 9. One of the main beam drift sources shown in Fig. 9 is due to the decrease in the quantum efficiency (QE) of the photocathode of this dc gun. The QE before the start of cw operation was approximately 4.2%, decreasing to approximately 3.4% after the operation. No HOM heating was observed in the main-linac cavities. The vacuum level of the beam dump was maintained at less than 10^{-5} Pa without significant heating in the dump section by rastering the beam, whereas the nominal vacuum level without beam irradiation of the dump was at the 10^{-7} Pa level. The beam drifted from 0.9 to 0.8 mA within a few hours. However, we maintained stable beam operation. Figure 10 shows the trend of the radiation measured by all ALOKA radiation monitors in the cERL during energy recovery at approximately 1 mA cw operation in Run 2 (shown in Fig. 9). ALOKA radiation monitors No. 5 and No. 6 were located immediately before and after the main-linac cryomodule, respectively [18]. Both monitors showed significant field emissions of approximately 100 mSv/h, which came from the main linac. In Fig. 10, the measured radiation in the monitors is plotted by subtracting the background level, which originates from the main-linac field emission. These field emission levels did not change with constant accelerating voltage. However, the large background of the field emission might have enhanced the fluctuation of radiation monitors No. 5 and No. 6, as shown in Fig. 10. After collimator tuning, we maintained a

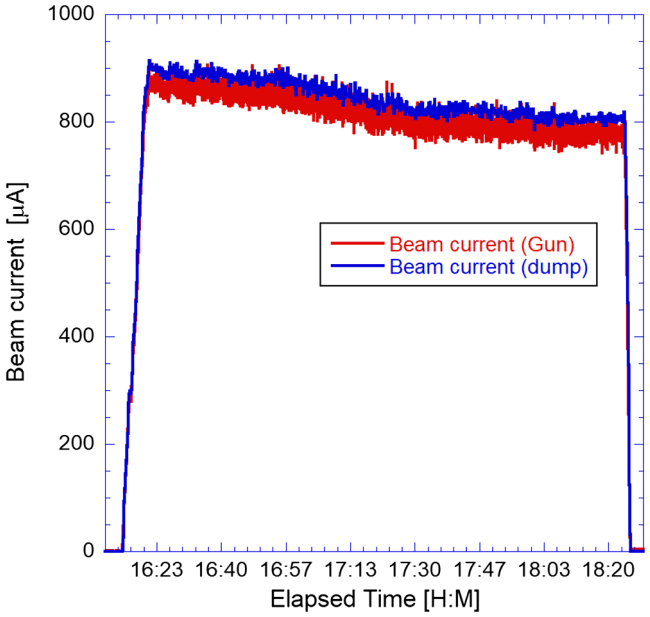

FIG. 9. Beam current trend during energy recovery at approximately 1 mA cw operation in Run 2. The solid red line shows the beam current measured at the dc gun. The blue line shows the measured beam current at the beam dump by Faraday cup. The horizontal (vertical) axis shows the elapsed time (beam current).

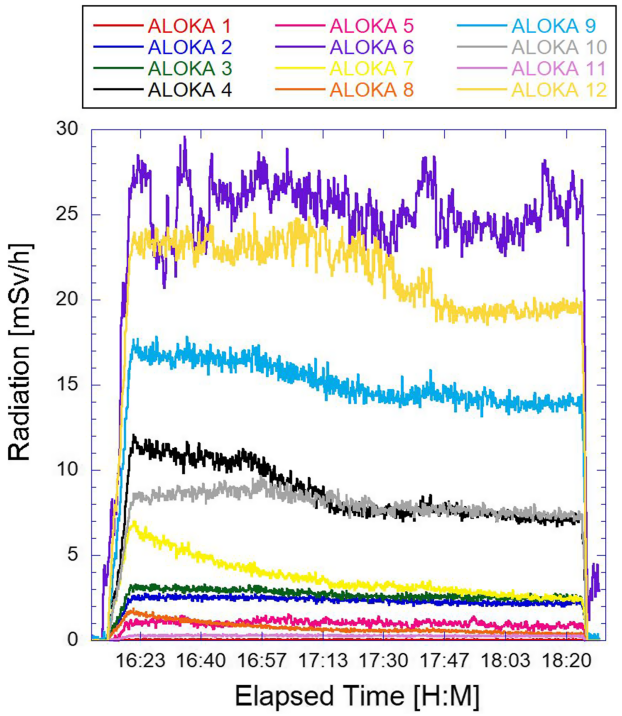

FIG. 10. Trend of all ALOKA radiation monitors during energy recovery at approximately 1 mA cw operation in Run 2, as shown in Fig. 9.

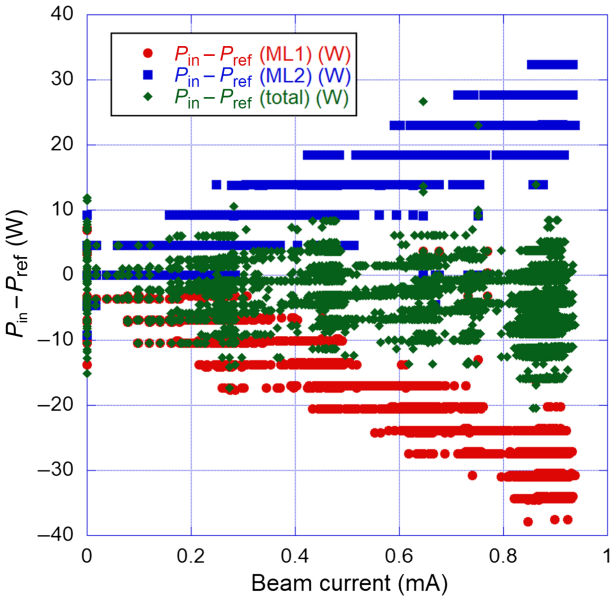

FIG. 11. Power variation ($P_{in} - P_{ref}$) in Run 1 with respect to the beam current. The horizontal axis shows the beam current (I). The vertical axis shows the variation of $P_{in} - P_{ref}$ from the zero-beam current. The $P_{in,cav} - P_{ref,cav}$ variations in each cavity (ML1 and ML2) are shown in red and blue, respectively. The variation of $P_{in} - P_{ref}$ for the sum of ML1 and ML2 is shown in green.

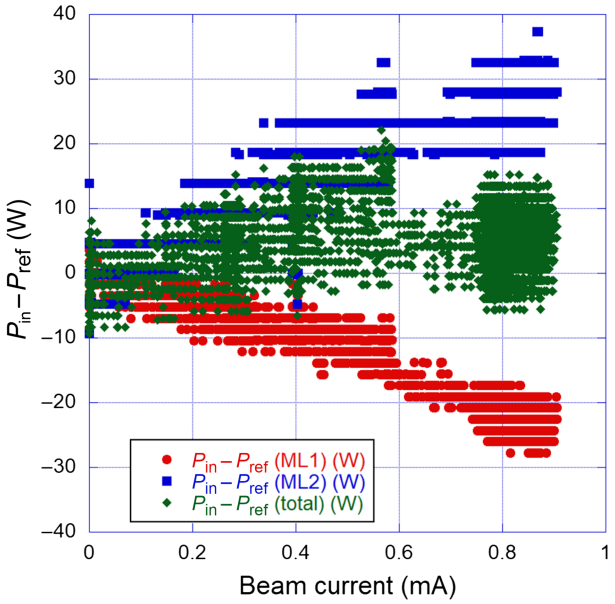

FIG. 12. Power variation ($P_{in} - P_{ref}$) in Run 2 with respect to the beam current. The horizontal axis shows the beam current (I). The vertical axis shows the variation of $P_{in} - P_{ref}$ from the zero-beam current. The $P_{in,cav} - P_{ref,cav}$ variations in each cavity (ML1 and ML2) are shown in red and blue, respectively. The $P_{in} - P_{ref}$ variation for the sum of ML1 and ML2 is shown in green.

low-radiation condition below 30 mSv/h in the cERL concrete shield. The drifts in the measured radiation of several ALOKA radiation monitors are shown in Fig. 9 as drifting beam currents. During this energy recovery operation, we did not observe a sharp increase in radiation due to a sudden beam kick or beam instabilities, such as the HOM-BBU. Notably, we maintained stable beam operation in Runs 1 and 3 under an approximately 1 mA cw beam energy recovery, despite observing the same drift for a few hours.

Figures 11–13 show the $P_{in} - P_{ref}$ variation during energy recovery in Runs 1, 2, and 3, respectively. The red and blue lines in these three figures show the ($P_{in,cav} - P_{ref,cav}$) differences in each cavity with respect to the beam current in ML1 and ML2, respectively. The green line in these three figures shows the ($P_{in} - P_{ref}$) variation with respect to the total ($P_{in} - P_{ref}$) of ML1 + ML2. We observed good linear responses between ($P_{in} - P_{ref}$) and the current I in Figs. 11–13. ε_{rf} was evaluated using a linear fit between ($P_{in} - P_{ref}$) and the beam current at each run. Notably, nonzero slopes of $(P_{in} - P_{ref})/I$ were observed in each cavity, as shown in Figs. 11–13. Due to the low-energy beam acceleration of the 2.9-MeV injection beam and deceleration of the 2.9-MeV beam to the damp, phase slip occurred despite maintaining a 100% energy-recovery condition. A detailed explanation of these phase slips is outlined in the Appendix.

Table III lists the energy recovery efficiencies in Figs. 11–13 for Runs 1, 2, and 3, respectively. Although

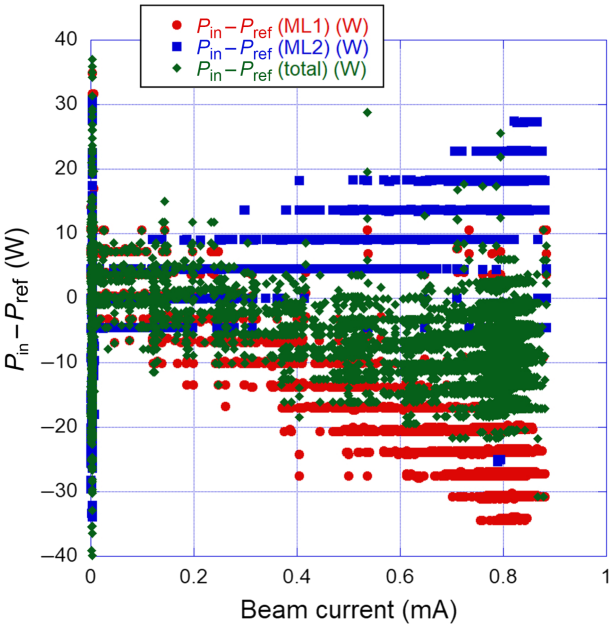

FIG. 13. Power variation ($P_{in} - P_{ref}$) in Run 3 with respect to the beam current. The horizontal axis shows the beam current (I). The vertical axis shows the $P_{in} - P_{ref}$ variation from the zero-beam current. The $P_{in,cav} - P_{ref,cav}$ variations in each cavity (ML1 and ML2) are shown in red and blue, respectively. The $P_{in} - P_{ref}$ variation for the sum of ML1 and ML2 is shown in green.

TABLE III. Measured energy recovery efficiency (ε_{rf}).

Beam condition	Total energy recovery efficiency (ε_{rf})
Run 1	$100.032\% \pm 0.031\%$
Run 2	$99.958\% \pm 0.035\%$
Run 3	$100.040\% \pm 0.035\%$

a deviation of less than 0.042% was observed in Runs 1, 2, and 3, the energy recovery rate was almost 100.00%, considering an error bar of 0.035%. The measured error bars in Table III are due to the accuracy of the power meter and the error of linearity of the power meters of P_{in} and P_{ref} (see details in the Appendix). Notably, we stably operated with an amplitude stability of less than 0.02% and phase stability of less than 0.02° for ML1 and ML2 during beam operation [23].

IV. DISCUSSION

A. Beam loss discussion

The accelerator in the cERL is surrounded by a concrete shield. If significant beam loss occurs, the generated photons reach the exterior of the concrete shield near the beam loss point. Therefore, the beam loss distribution along the beamline in the cERL reflects the photon dose rate distribution on the roof of the cERL concrete shield. A high-current operation was achieved by suppressing this beam loss in the cERL. Therefore, we estimated the beam loss location and beam loss current during an energy recovery operation of approximately 1 mA by measuring the photon dose rates on the concrete roof. Figure 14 shows the measured photon dose rate distribution for Run 1. A 1-inch NaI(Tl) scintillation survey meter (Aloka, TCS-171B) was used for these measurements. A maximum value of 0.23 μSv/h was measured on the concrete roof on the north straight line.

The photon dose rate per beam loss current was calculated using the MARS15 code to estimate the beam loss current corresponding to the measured photon dose rate on the concrete roof [24,25]. In the case of beam loss in a magnet, we assumed that the 20 MeV electrons collided with the beam chamber at a 1° angle in the center of the magnet. For beam loss in a collimator, we assumed that the electrons collided head-on with the collimator. An example of the MARS15 calculation results is shown in Fig. 15. The maximum photon dose rate appeared slightly downstream from the beam loss point, as shown in Fig. 15. In this case, a beam loss of 1 nA leads to a photon dose rate of 0.027 μSv/h on the roof of the cERL room downstream from the chicane magnets. The calculation results of the 17.5-MeV beam are similar to those of the 20-MeV beam. Therefore, we applied the simulation results to the 17.5- and 20.0-MeV cases.

For Run 1, the maximum measured radiation was 0.23 μSv/h on the roof downstream of the main linac, as shown in Fig. 14. If we apply the beam loss estimation, as shown in Fig. 15, near the maximum radiation point of 0.23 μSv/h with the same thickness of the roof at this point, the beam loss current can be roughly estimated to be $(0.23\,\mu\text{Sv/h})/(0.027\,\mu\text{Sv/h}) \times 1\,\text{nA} = 9\,\text{nA} = 0.009\,\mu\text{A}$ at this point. The loss ratio of 0.9 mA (900 μA) was found to be 0.009 μA/900 μA = 0.001%. The energy-recovery

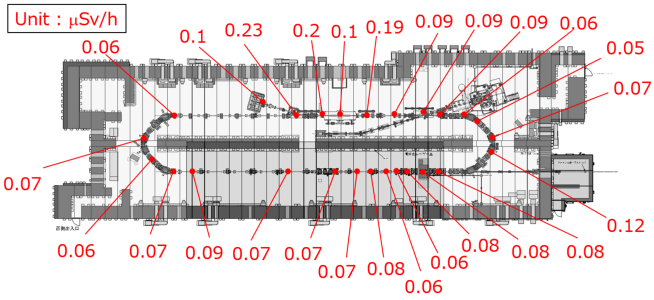

FIG. 14. The measured photon dose rate distribution on the concrete roof in Run 1. The photon dose rate values include a background value of 0.05 μSv/h. The beam current was between 0.8 and 0.9 mA.

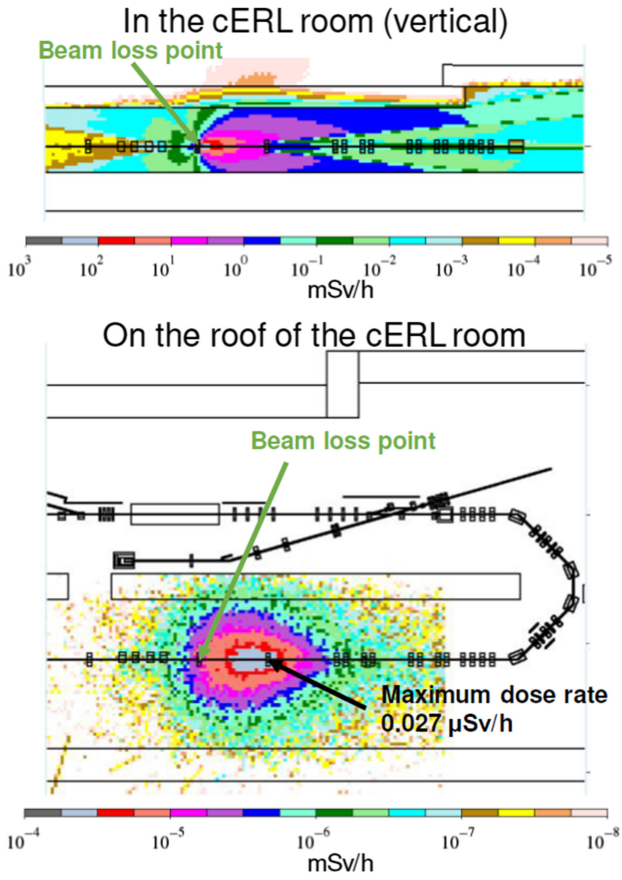

FIG. 15. Example of the dose rate distribution calculated using MARS15. In this calculation, 1-nA beam loss occurred in the center of the magnet [24].

efficiency was $100.032\% \pm 0.031\%$ in Run 1. We did not compare the actual beam loss estimates because the local loss point was not measured in Run 1. However, the total loss was estimated by $(1 - \varepsilon_{\mathrm{rf}})$, and the loss estimation of 0.001% by the simulation of MARS15 from the measured maximum values of 0.23 μSv/h, as shown in Fig. 14, was estimated to be nearly consistent with $-0.032\% \pm 0.031\%$ of $(1 - \varepsilon_{\mathrm{rf}})$. Multiple dose meters must be set along the cERL beamline to estimate the detailed beam loss distribution.

Other energy losses occurred when the beam current increased. With respect to the HOM heat load during the approximately 1-mA operation, the HOM heat load is calculated using our design value of 10 V/pC with a 3-ps bunch length of the loss factor of the HOM in the main linac [19]. In Runs 1 and 2, the calculated HOM heat load was 6.3 mW, and in Run 3, the calculated HOM heat load was 54 mW. These HOM heat loads contributed little to the energy-recovery efficiency. These heat loads resulted in no HOM heating during the energy recovery operation of approximately 1 mA.

We concluded that an energy recovery efficiency of almost 100.00% can be achieved by eliminating losses at all locations along the beamline in the cERL when energy recovery is successful, as demonstrated in Run 1.

B. Emittance measurement discussion

In Runs 1 and 2, high-efficiency energy-recovery operation of approximately 1 mA was achieved with a very small emittance of 0.2–0.4 mm mrad. These values are also close to the measurement results shown in Ref. [15], indicating that the space-charge effect is negligible, even when the charge increases to 0.7 pC/bunch. Conversely, higher emittances of approximately 1–2 mm mrad were obtained in Run 3, where energy recovery was performed at 5.5 pC/bunch. These emittance growths are mainly due to space-charge effects [26]. In particular, the calculated emittance was 2.9 mm mrad in the horizontal direction and 1.8 mm mrad in the vertical direction when the emittance was calculated in the case of Run 3 optics with a beam of 7.7 pC/bunch at the south-straight section. These values are similar to the measured values in Table II for Run 3. The energy recovery operation was possible with an emittance as small as a few mm mrad, which is close to the design of Run 3. For future 10-mA energy recovery operations, the cERL can be operated at 7.7 pC/bunch at 1.3 GHz. If the beam optics are the same as that in Run 3 for a 10-mA energy recovery operation, energy recovery without beam loss will be possible.

V. CONCLUSION

This study investigates energy-recovery operations with a cERL at approximately 1 mA. Three energy-recovery runs were performed under three different conditions. We performed beam tuning with low emittance and extremely small beam loss before cw operation by optimum beam tuning and by effectively using the collimator and loss monitor. The measured emittances were as small as 0.2–0.4 mm mrad at 0.7 pC/bunch. Furthermore, even at 5.5 pC/bunch operation, a low emittance of 2 mm mrad was achieved. After switching to cw operation, extremely high-efficiency energy-recovery operations of $100.0\% \pm 0.04\%$ were achieved in three energy-recovery runs at an approximately 1-mA beam. This 100.0% level of energy recovery reduced the beam loss and achieved very low radiation conditions.

This method, which efficiently utilizes collimators and loss monitors, achieves 100.0% energy-recovery efficiency at a high current of 1 mA, characterized by low emittance and extremely small beam loss. In particular, the realization of energy recovery at 5.5 pC/bunch shows the feasibility of future 10-mA high-current operations with an extremely high energy-recovery efficiency. The findings of this study provide insights into steady beam operation for high-brightness beams and high-efficiency energy recovery operations required for future extreme ultraviolet free-electron lasers (EUV-FELs) [7] and other applications. EUV-FELs are operated under off-crest conditions with less than a 10° phase difference from the on-crest condition. Future studies will focus on investigating cw ERL operation under off-crest conditions for EUV-FELs.

ACKNOWLEDGMENTS

We would like to thank Hiroshi Kawata, Yukinori Kobayashi, and Shinichiro Michizono for their continuous encouragement of the cERL beam operation. We thank the cERL members for their support with the beam operation. This work was partially supported by the Government (MEXT) Subsidy for Strengthening Nuclear Security and the Quantum Beam Technology Program of the Japanese Ministry of Education, Culture, Sports, Science, and Technology (MEXT).

DATA AVAILABILITY

The data are not publicly available. The data are available from the authors upon reasonable request.

APPENDIX: CONSIDERATION OF ENERGY RECOVERY OF EACH MAIN-LINAC CAVITY

In the cERL, the $(P_{\mathrm{in,cav}} - P_{\mathrm{ref,cav}})$ of ML1 and ML2 had small slopes with respect to beam current, as shown in Figs. 11–13. If the beam energy is sufficiently high, then the beam velocity is close to the speed of light. In this case, energy recovery is perfectly established, and no current dependence appears. The total injection energy at a cERL of 2.9 MeV is extremely low, and the beam does not reach the speed of light under acceleration by the main linac. This causes a phase slip during acceleration and deceleration,

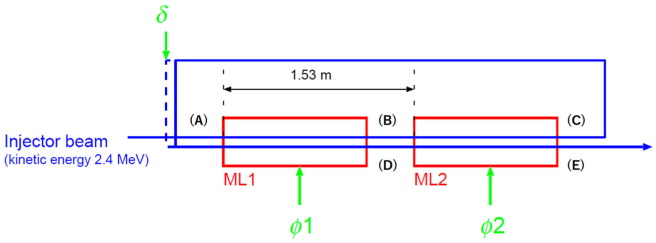

FIG. 16. The calculation setup layout of cERL under energy-recovery conditions.

resulting in slightly different efficiencies for each cavity [27,28]. We performed a particle-tracking simulation in a simple mode to confirm whether the measured nonenergy recovery rate was reasonable.

Figure 16 shows the setup for calculations. A beam with an injection energy of 2.9 MeV (kinetic energy of 2.4 MeV) was injected into the main linac, which was based on two 1.3-GHz nine-cell cavities of the ERL-model-2 cavity (ML1, ML2) [18,19]. Figure 17 shows the electrical field profile of the main linac along the beam axis, defined as E_z. The distance between the centers of the upstream (ML1) and downstream cavities (ML2) was 1.53 m. The amplitude and phase of each cavity were controlled independently. After acceleration in the two cavities, the beam was delayed in the recirculation loop, injected into ML1, and tracked to the exit of ML2. The phase of the beam after the orbit was adjusted using the delay length, and the phase relationship between the two cavities was fixed.

The calculation setup was similar to that for the cERL accelerator. The procedure is as follows: (i) The phase of ML1 ($\phi 1$) is scanned and set to the phase in which the energy is maximum at the ML1 exit during acceleration (on crest). (ii) The ML2 phase ($\phi 2$) is scanned and set to the phase where the energy is maximum at the ML2 exit during acceleration (on crest). (iii) The "delay" of the recirculation

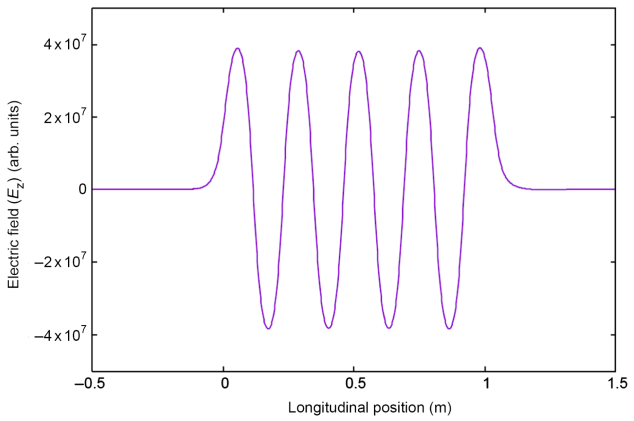

FIG. 17. The electrical field profile of the cERL main linac. The horizontal and vertical axes show the longitudinal position along the beam axis in the cavity and the electrical field of the beam direction (arbitrary unit), respectively.

loop (δ) is adjusted and set so that the energy at the ML2 exit is minimized after deceleration without changing the phases of $\phi 1$ and $\phi 2$. (iv) The beam energy is calculated, and the kinetic energy at each point is obtained [(A)–(E) in Fig. 16] after adjusting the phase and delay length.

The kinetic energy of the cERL injection beam was 2.4 MeV and that of the beam after acceleration on the linac was 19.4 MeV. A total of 17.0 MeV was obtained in the main linac and accelerated in the main-linac cavities. Table IV shows the calculated energies at positions (A)–(E) for ML1 and ML2 with an 8.5-MV amplitude. The accelerating energy of ML1 was obtained from the energy difference between (A) and (B), that of ML2 was obtained from the energy difference between (B) and (C), and the energy difference between (C) and (D) provides the deceleration energy of ML1. The energy difference between positions (D) and (E) provides the deceleration energy of ML2.

The energy recovery efficiency is defined in Eq. (2). By contrast, the inefficiency of energy recovery ($\varepsilon_{\mathrm{rf\_ineff}}$) is defined using Eq. (A1) for a clearer comparison.

$$\varepsilon_{\mathrm{rf\_ineff}}(\%) = (1-\varepsilon_{\mathrm{rf}})(\%) = (P_{\mathrm{in}} - P_{\mathrm{ref}})/P_{\mathrm{rf,acc}} \times 100\% \tag{A1}$$

Equation (A1) defines the energy-recovery inefficiency of cERL operation. By estimating the inefficiency of the energy recovery in each cavity of ML1 and ML2, we can replace P_{in} (P_{ref}) of each cavity in Eq. (A1) with $P_{\mathrm{in,cav}}$ ($P_{\mathrm{ref,cav}}$), and $P_{\mathrm{rf,acc}}$ with the beam power of each cavity as $V_c \times I$. From the balance of the cavity acceleration under the energy-recovery condition, we can redefine the inefficiency of the energy recovery as follows:

$$\varepsilon_{\mathrm{rf\_ineff}}(\%) = (V_{\mathrm{c\_acc}} + V_{\mathrm{c\_dec}})/[(V_{\mathrm{c\_acc}} - V_{\mathrm{c\_dec}})/2] \times 100\%, \tag{A2}$$

where $V_{\mathrm{c\_acc}}$ ($V_{\mathrm{c\_dec}}$) is the acceleration (deceleration) gain of each cavity. This implies that for ML1, $V_{\mathrm{c\_acc}}$ is the gain obtained from (A) to (B), and $V_{\mathrm{c\_dec}}$ is the gain obtained from (C) to (D). For ML2, $V_{\mathrm{c\_acc}}$ is the gain obtained from (B) to (C), and $V_{\mathrm{c\_dec}}$ is the gain obtained from (D) to (E).

TABLE IV. Energy gain calculation of each cavity on the main linac under energy recovery conditions at the cERL.

Position	Kinetic energy (MeV)	Gain of each cavity (MV)
(A)	2.4000	
(B)	10.8805	8.4805 (ML1)
(C)	19.4034	8.5229 (ML2)
(D)	10.8797	−8.5238 (ML1)
(E)	2.4003	−8.4794 (ML2)

TABLE V. Comparison between the measured energy-recovery inefficiency in Runs 1 and 3 and the calculated energy-recovery inefficiency.

Experimental results (total energy of 20 MeV)			
Energy-recovery inefficiency ($\varepsilon_{\mathrm{rf\_ineff}}$)	Run 1	Run 3	Calculation (%)
ML1	$-0.391\% \pm 0.047\%$	$-0.453\% \pm 0.054\%$	-0.509
ML2	$+0.326\% \pm 0.039\%$	$+0.374\% \pm 0.044\%$	$+0.512$
Total	$-0.032\% \pm 0.031\%$	$-0.040\% \pm 0.035\%$	$+0.0018$

A comparison of the calculated and measured energy inefficiencies of energy recovery for each cavity and the total is shown in Table V. The measured values in Table V were used in Runs 1 and 3, as shown in Figs. 11 and 13, respectively. In addition, the inefficiency of the energy recovery ($\varepsilon_{\mathrm{rf\_ineff}}$) was obtained from the ($P_{\mathrm{in}} - P_{\mathrm{ref}}$) variation at the maximum beam current and ($P_{\mathrm{in}} - P_{\mathrm{ref}}$) at zero current, as shown in Figs. 11 and 13.

The measurement results showed energy-recovery inefficiencies of 0.3%–0.5% in each cavity. Conversely, the calculations showed inefficiencies of approximately 0.51%. One of the inefficiency measurements of ML1 in Run 1 agrees well with the calculation within the error bar. However, the remaining measurement results for the inefficiencies in each cavity are slightly lower than the expected values. Some unknown systematic factors or errors remain under the cERL condition. For example, the fringe fields from ML1 and ML2 were larger, and the calculated inefficiency was larger. However, the measurement results were not significantly different from the calculation results. Therefore, approximately 100.0% energy recovery was achieved in the measurement and calculation results.

[1] M. Tigner, A possible apparatus for electron clashing-beam experiments, Nuovo Cimento **37**, 1228 (1965).

[2] A. Hutton, Energy-recovery linacs for energy-efficient particle acceleration, Nat. Rev. Phys. **5**, 708 (2023).

[3] W. Kaabi *et al.*, PERLE: A high power energy recovery facility, in *Proceedings of the 10th International Particle Accelerator Conference (IPAC2019), Melbourne, Australia, 2019* (JACoW, Geneva, Switzerland, 2019), pp. 1396–1399, 10.18429/JACoW-IPAC2019-TUPGW008.

[4] F. Hug, K. Aulenbacher, R. G. Heine, B. Ledroit, and D. Simon, MESA—An ERL project for particle physics experiments, in *Proceedings of LINAC2016, East Lansing, MI, 2016* (JACoW Publishing, Geneva, Switzerland, 2017), pp. 313–315, 10.18429/JACoW-LINAC2016-MOP106012.

[5] A. Bartnik *et al.*, CBETA: First multipass superconducting linear accelerator with energy recovery, Phys. Rev. Lett. **125**, 044803 (2020).

[6] K.-J. Kim, Y. Shvyd'ko, and S. Reiche, A proposal for an x-ay free-electron laser oscillator with an energy-recovery linac, Phys. Rev. Lett. **100**, 244802 (2008).

[7] H. Kawata, N. Nakamura, H. Sakai, R. Kato, and R. Hajima, High power light source for future extreme ultraviolet lithography based on energy-recovery linac free-electron laser, J. Micro/Nanopattern. Mater. Metrol. **21**, 021210 (2022).

[8] T. Akagi, A. Kosuge, S. Araki, R. Hajima, Y. Honda, T. Miyajima, M. Mori, R. Nagai, N. Nakamura, M. Shimada, T. Shizuma, N. Terunuma, and J. Urakawa, Narrow-band photon beam via laser Compton scattering in an energy recovery linac, Phys. Rev. Accel. Beams **19**, 114701 (2016).

[9] I. Drebot *et al.*, BriXSinO high-flux dual x-ray and THz radiation source based on energy recovery linacs, in *Proceedings of the 13th International Particle Accelerator Conference (IPAC2022), Bangkok, Thailand, 2022* (JACoW Publishing, Geneva, Switzerland, 2023), pp. 2407–2410, 10.18429/JACoW-IPAC2022-THOXSP2.

[10] R. Hajima, T. Shizuma, M. Sawamura, R. Nagai, N. Nishimori, N. Kikuzawa, and E. J. Minehara, First demonstration of energy-recovery operation in the JAERI superconducting linac for a high-power free-electron laser, Nucl. Instrum. Methods Phys. Res., Sect. A **507**, 115 (2003).

[11] G. R. Neil *et al.*, The JLab high power ERL light source, Nucl. Instrum. Methods Phys. Res., Sect. A **557**, 9 (2006).

[12] O. A. Shevchenko *et al.*, The Novosibirsk free electron laser facility, AIP Conf. Proc. **2299**, 020001 (2020).

[13] F. Schliessmann, M. Arnold, L. Juergensen, N. Pietralla, M. Dutine, M. Fischer, R. Grewe, M. Steinhorst, Lennart Stobbe, and S. Weih, Realization of a multi-turn energy recovery accelerator, Nat. Phys. **19**, 597 (2023).

[14] B. Dunham *et al.*, Record high-average current from a high-brightness photoinjector, Appl. Phys. Lett. **102**, 034105 (2013).

[15] M. Akemoto *et al.*, Construction and commissioning of the compact energy-recovery linac at KEK, Nucl. Instrum. Methods Phys. Res., Sect. A **877**, 197 (2018).

[16] N. Nishimori, R. Nagai, S. Matsuba, R. Hajima, M. Yamamoto, T. Miyajima, Y. Honda, H. Iijima, M. Kuriki, and M. Kuwahara, Generation of a 500-keV electron beam from a high voltage photoemission gun, Appl. Phys. Lett. **102**, 234103 (2013).

[17] K. Watanabe, S. Noguchi, E. Kako, K. Umemori, and T. Shishido, Development of the superconducting rf 2-cell cavity for cERL injector at KEK, Nucl. Instrum. Methods Phys. Res., Sect. A **714**, 67 (2013).

[18] H. Sakai, E. Cenni, K. Enami, T. Furuya, M. Sawamura, K. Shinoe, and K. Umemori, Field emission studies in vertical

test and during cryomodule operation using precise x-ray mapping system, Phys. Rev. Accel. Beams **22**, 022002 (2019).

[19] H. Sakai, K. Shinoe, T. Furuya, S. Sakanaka, T. Suwada, T. Takahashi, K. Umemori, and M. Sawamura, Development of a 1.3 GHz 9-cell superconducting cavity for the energy recovery linac, in *Proceedings of the 41st Advanced ICFA Beam Dynamics Workshop on Energy Recovery Linacs (ERL07), Daresbury, UK, 2007* (JACoW, Geneva, Switzerland, 2007), pp. 56–61, https://proceedings.jacow.org/erl07/papers/34.pdf.

[20] T. Miyajima, Y. Honda, R. Takai, T. Obina, M. Shimada, K. Harada, M. Yamamoto, K. Umemori, H. Sakai, T. Miura, F. Qiu, N. Nakamura, S. Sakanaka, N. Nishimori, R. Nagai, R. Hajima, and D. Lee, Status of higher bunch charge operation in compact ERL, in *Proceedings of the 6th International Particle Accelerator Conference (IPAC2015), Richmond, VA, 2015* (JACoW, Geneva, Switzerland, 2015), pp. 1583–1586, 10.18429/JACoW-IPAC2015-TUPWA067.

[21] O. Tanaka, N. Nakamura, M. Shimada, T. Miyajima, A. Ueda, T. Obina, and R. Takai, New halo formation mechanism at the KEK compact energy recovery linac, Phys. Rev. Accel. Beams **21**, 024202 (2018).

[22] M. Arnold, T. Bahlo, M. Dutine, R. Grewe, J. H. Hanten, L. E. Jürgensen, J. Pforr, N. Pietralla, F. Schließmann, M. Steinhorst, and S. Weih, ERL operation of S-DALINAC, in *Proceedings of the 63rd ICFA Advanced Beam Dynamics Workshop on Energy Recovery Linacs (ERL2019), Berlin, Germany, 2019* (JACoW, Geneva, Switzerland, 2019), pp. 1–4, 10.18429/JACoW-ERL2019-MOCOXBS02.

[23] F. Qiu, T. Matsumoto, S. Michizono, and T. Miura, Development of MicroTCA-based low-level radio frequency control systems for cERL and STF, in *Proceedings of the 12th International Workshop on Emerging Technologies and Scientific Facilities Controls (PCaPAC2018), Hsinchu, Taiwan, 2018* (JACoW, Geneva, Switzerland, 2019), pp. 124–126, 10.18429/JACoW-PCaPAC2018-THCA2.

[24] H. Matsumura, A. Toyoda, S. Sakanaka, K. Haga, T. Obina, T. Miura, K. Hozumi, S. Nagaguro, T. Oyama, and N. Yoshihara, Beam loss estimation by measurement of secondarily produced photons under high average-current operations of compact ERL in KEK, in *Proceedings of 7th International Particle Accelerator Conference, IPAC-2016, Busan, Korea, 2016* (JACoW, Geneva, Switzerland, 2016), pp. 2711–2714, WEPOR020, 10.18429/JACoW-IPAC2016-WEPOR020.

[25] N. V. Mokhov and S. I. Striganov, MARS15 overview, AIP Conf. Proc. **896**, 50 (2007).

[26] T. Miyajima, Y. Honda, M. Shimada, R. Takai, T. Obina, K. Harada, M. Yamamoto, N. Nakamura, K. Umemori, E. Kako, T. Miura, R. Kato, T. Hotei, R. Nagai, R. Hajima, and N. Nishimori, 60 pC bunch charge operation of the compact ERL at KEK, in *Proceedings of 8th International Particle Accelerator Conference, IPAC2017, Copenhagen, Denmark, 2017* (JACoW, Geneva, Switzerland, 2017), pp. 890–893, 10.18429/JACoW-IPAC2017-MOPVA019.

[27] R. Koscica, N. Banerjee, G. H. Hoffstaetter, W. Lou, and G. Premawardhana, Energy and rf cavity phase symmetry enforcement in multiturn energy recovery linac models, Phys. Rev. Accel. Beams **22**, 091602 (2019).

[28] M. Arnold, J. Birkhan, J. Pforr, N. Pietralla, F. Schließmann, M. Steinhorst, and F. Hug, First operation of the superconducting Darmstadt linear electron accelerator as an energy recovery linac, Phys. Rev. Accel. Beams **23**, 020101 (2020).